Electric Field Integral Equation Formulation For a Dynamic Analysis of Nonuniform Microstrip Multi-Conductor Transmission Lines

Tawfik Rahal Arabi, *Student Member, IEEE,* Arthur T. Murphy, *Fellow, IEEE,* and Tapan K. Sarkar, *Fellow, IEEE*

Abstract—**The objective of this paper is to present a numerical technique based on a combined approach of using a "quasi-dynamic," a "dynamic" and an asymptotic approach for the analysis of nonuniform microstrip transmission lines and discontinuities using the grounded dielectric slab Green's functions. The regions of validity of the quasi-dynamic and asymptotic approximations have been determined in terms of the required accuracy in the Green's functions. Finally, numerical examples have been presented and checked with available data to check the accuracy of this new technique.**

I. Introduction

THIS PAPER describes an Electric Field Integral Equation Formulation (EFIEF) for the dynamic characterization of nonuniform microstrip transmission lines and discontinuities. In the dynamic approach, the Green's functions are Sommerfeld type integrals that can be evaluated only numerically. The crucial element to a numerical advantage of the EFIEF therefore, lies in the efficient computation of the Green's functions, particularly in the analysis of electrically large structures. In this paper, the quasi dynamic approximation [1]–[3] has been used for the near field and the asymptotic steepest descent approximation for the far field calculations. The regions of validity of the quasi-dynamic and asymptotic approximations are determined in terms of the microstrip physical parameters and the required accuracy.

Section II of this paper deals with the moment method formulation of the problem. For multi-conductor transmission lines, a new approach of utilizing the transversal quasistatic distribution for the transversal component of the current has been described.

Section III deals with the circuit parameters extraction from the current and voltage distributions. Several examples have been solved in order to demonstrate the usefulness of the technique. Finally the conclusion is presented in Section IV.

Manuscript received on August 8, 1991; revised January 22, 1992. This work was supported in part by a research grant from E.I. DuPont De Nemours & Company, and by grant for supercomputer time from the Cornell National Science Foundation SuperComputing Facility.

T. Arabi is with Intel Corporation, Architecture Development Lab, 5200 N. E. ElamYoung Parkway, Hillsboro, OR 97124.

A. T. Murphy is with DuPont Electronics, E. E. DuPont De Nemours & Company, Experimental Station, Wilmington, DE 19880.

T. K. Sarkar is with the Department of Electrical Engineering at Syracuse University, Syracuse, NY 13244.

IEEE Log Number 9201712.

II. Moment Method Formulation

For the most general planar structures, the current distribution is a two dimensional current with both longitudinal and transversal flows. For most transmission lines-like structures however, the transversal component of the current is negligible compared to the longitudinal component and the current may be assumed to flow in the axial direction only [1], [4]. Such an assumption leads to a considerably more efficient moment method solution as it substantially reduces the generalized impedance matrix size. Thus considering the microstrip multi-conductor transmission line of Fig. 1, the current distribution on each metallic conductor may be written as:

$$\vec{J}_s = \sum_{i=1}^{N} a_i Q_i(y') T_i(x') \vec{e}_x \tag{1}$$

where $T_i(x')$ is a triangular element defined as

$$T_i(x') = \begin{cases} 1 + \dfrac{x}{x_2} & -x_2 \le x \le 0 \\ 1 - \dfrac{x}{x_2} & 0 \le x \le x_2 \\ 0 & \text{elsewhere} \end{cases}$$

Here it was assumed that the current element is locally oriented in the $\vec{x}$ direction and the origin of the coordinates coincide with the mid point of the interval $[-x_2, x_2]$ over which the current element is defined (Fig. 2). The transversal current distribution $Q_i(y')$ is assumed to be known. The moment method generalized impedance elements for such distribution can be written as [1], [2]

$$Z_{ij} = \int_{W_j} dy_j \int_{W_i} dy' \int_{l_j} dx_j \int_{l_i} dx' Q_i(y') Q_j(y_j) * \begin{Bmatrix} [C_1 G_1(x, y, x', y') T_n(x') T_m(x_j) \vec{e}_x \cdot \vec{e}_{x_j}] \\ + C_2 G_2(x, y, x', y') \\ \cdot \left[\dfrac{\partial}{\partial x'} T_n(x') + \dfrac{\partial}{\partial x_j} T_m(x_j)\right] \end{Bmatrix} \tag{2}$$

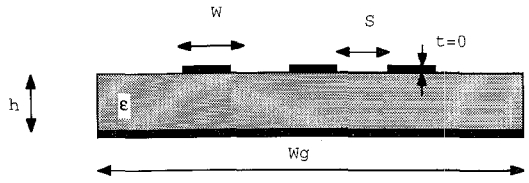

Fig. 1. Shows a 3 conductor microstrip transmission line where W is the line width, S is the separation between conductors, t is the conductor thickness, h is the dielectric height and ϵ is the complex dielectric constant.

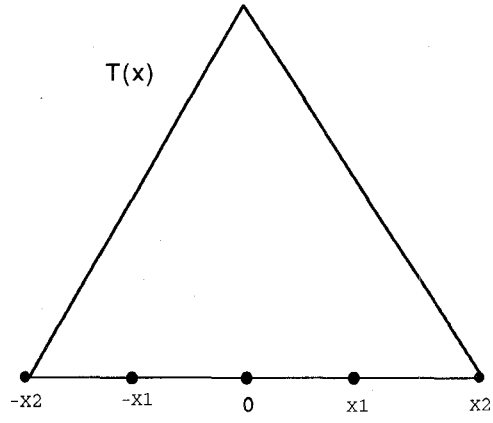

Fig. 2. Shows the triangular basis functions for the longitudinal component of the current distribution.

where G_1 and G_2 are the Sommerfeld type Green's functions of the problem and C_1, C_2, G_1, G_2 have been given in [1], [5]. For completeness, they are also given in Appendix A. The generalized voltage vector elements are given by

$$V_j = \langle E_i;\, Q_j(y')\, T_j(x') \rangle. \tag{3}$$

The transversal current distribution $Q_i(y')$ depends on the microstrip geometrical data. Thus for a single narrow line, that is a line such that (W/H) is small (*typically*, $(W/H) \leq 0.1$), the transversal current distribution has a square root behavior [1, 4, 6] and can be replaced with a cylindrical wire of equivalent radius ($a = [W/4]$) [7]. The current may thus be assumed filamentary and flowing in the axis of the cylinder only. The boundary condition of zero tangential electric field is then applied at the surface of the cylindrical wire. For such a distribution, the generalized impedance matrix elements may be further simplified to:

$$Z_{ij} = \int_{l_j} dx_j \int_{l_i} dx' = \left\{ \begin{array}{l} G_1(x, y, x', y')\, T_n(x')\, T_m(x_j)\, \vec{e}_x \cdot \vec{e}_{x_j} \\ G_2(x, y, x', y') \left[\dfrac{\partial}{\partial x'} T_n(x') + \dfrac{\partial}{\partial x_j} T_m(x_j) \right] \end{array} \right\}.$$

For microstrip lines where (W/H) is large (typically, $(W/H) \geq 1$), the transversal current distribution is approximately constant over the strip width [1], [2], [6]. It may thus be written as:

$$\vec{J}_s = \sum_{i=1}^{N} \frac{1}{W} T_i(x')\, \vec{e}_x \tag{4}$$

For the intermediate region, the current distribution is assumed to follow the square root behavior. Therefore, for a single microstrip line, the transversal current distribution may be assumed known for all values of (W/H). For a multi-conductor line however, the transversal current distribution on each of the lines can no longer be approximated by a square root or a constant distribution due to the edge effects. The transversal distribution also depends on the location and number of excited lines. For example Figs. 3(a)–(c) show the current distribution on the three microstrip line of Fig. 1 for different values of (W/H) and different spacings (S/W). In these plots, the current distributions for conductors 1, 2, and 3 have been plotted on the intervals [0–20], [30–50], and [60–80] respectively. It is obvious from these figures that the square root behavior is not valid, particularly on the lines adjacent to the excited line except for very large (S/W) (typically $(S/W) \geq 10$). Thus if the spacing is very large and (W/H) is small, the lines may be approximated by wires of equivalent radii equal to $(1/4)$ of the strip widths. If (W/H) and (S/W) are both large, the current distribution may then be assumed constant on all lines. For the most general case, that is an arbitrary (W/H) and arbitrary (S/W), the transversal current distribution is obtained by solving the equivalent 2D problem involving the charge distribution [8], [9]. The equivalence of the charge and current distributions for the uniform, infinite length, multi-conductor transmission line has been shown in [9]. The exact numerical evaluation of the dynamic Green's functions involves a numerical computation of Sommerfeld type integrals [3], [10], [11]. The location of the zeros of the TE and TM microstrip transcendental equations have to be very accurately determined [12], [13] and extracted from the integrands. In this paper a combined (Newton–Raphson, bisection root) search has been unutilized to locate the zeros to within any specified accuracy. The numerical integration is then performed in essentially the same manner as described in [3], [10], [11].

2.1 The Quasi-Dynamic Approximation for the Green's Functions

In this paper, the quasi-dynamic approximations G_{1q} and G_{2q} are defined as

$$G_{1q}(\rho) = \lim_{k_1 \to 0} G_1(\rho) \tag{5}$$

$$G_{2q}(\rho) = \lim_{k_1 \to 0} G_2(\rho) \tag{6}$$

and are thus given by [1], [2], [3], [10]:

$$G_{1q}(\rho) = \frac{e^{-jk_1 r_0}}{r_0} - \frac{e^{-k_1 r_1}}{r_1} \tag{7}$$

$$G_{2q}(\rho) = (1 - \eta) \left\{ \frac{e^{-jk_1 r_1}}{r_1} - (1 + \eta) \cdot \sum_{i=1}^{i=\infty} (-\eta)^{(i-1)} \frac{e^{jk_1 r_i}}{r_i} \right\} \tag{8}$$

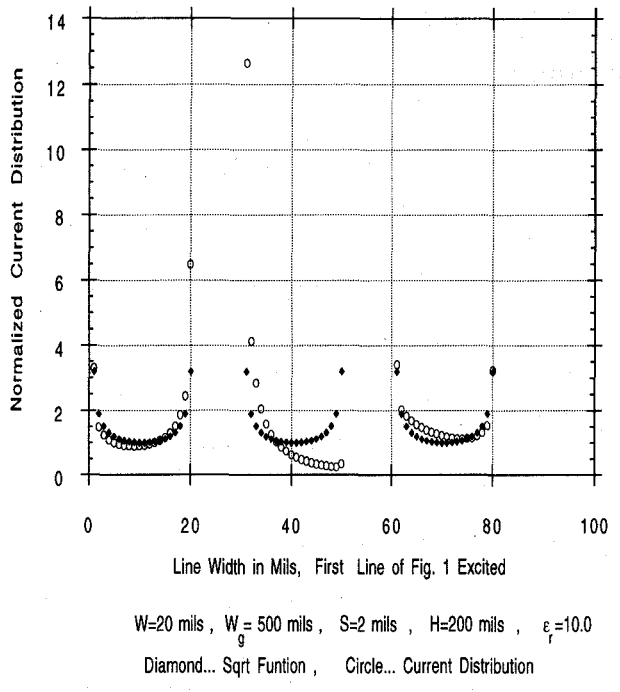

(a)

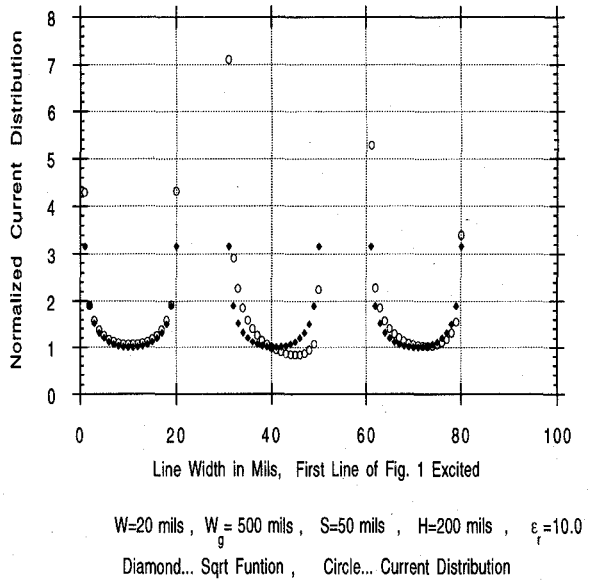

(b)

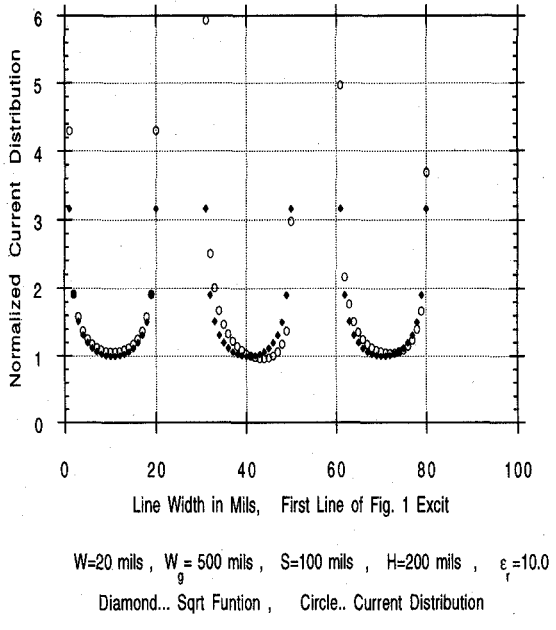

(c)

Fig. 3. (a)–(c) Shows a comparison between the normalized transversal distribution of the longitudinal current on each of the 3 conductors of Fig. 1 and the square root distribution. [0–20] Conductor 1, [30–50] Conductor 2, [60–80] Conductor 3.

where

$$\eta = \frac{1 - \epsilon_r}{1 + \epsilon_r} \tag{9}$$

$$r = \sqrt{\rho^2 + z^2}. \tag{10}$$

When the substrate height h is very small compared to both, the wavelength of operation and the source-to-field distance (ρ), G_{1q} may be written as

$$G_{1q}(\rho) = 2jh^2k_1 \frac{e^{-jk_1 r_0}}{r_0^2} + \text{higher order terms.} \tag{11}$$

In this paper we define the region of validity of the quasi-dynamic approximation $G_{iq}(\rho)$ by the radius (R_{iq}) such that

$$\left| \frac{G_i(\rho) - G_{iq}(\rho)}{G_i(\rho)} \right| \leq \text{error for all } \rho \leq R_{iq} \tag{12}$$

where *error* is any specified error tolerance. To illustrate, Figs. 4(a)–(b) show R_{1q} and R_{2q} as functions of the substrate heights h for different values of ϵ_r and an error tolerance of 0.05. It should be noted, that the quasi-dynamic approximations may as well be defined in terms of k_2 or

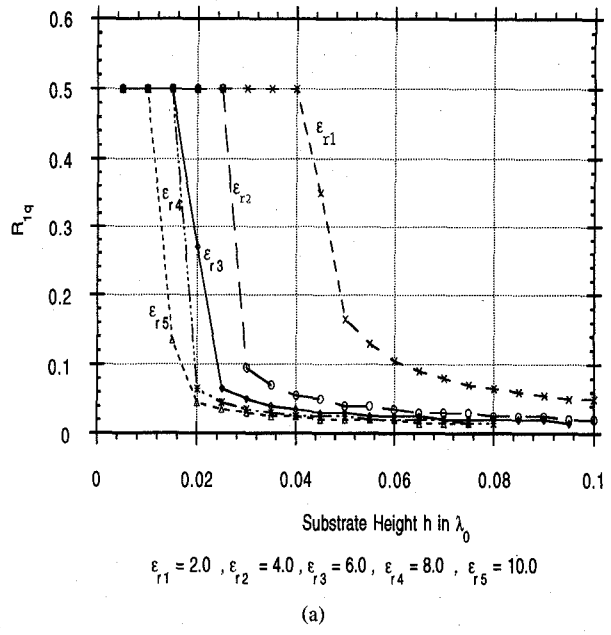

(a)

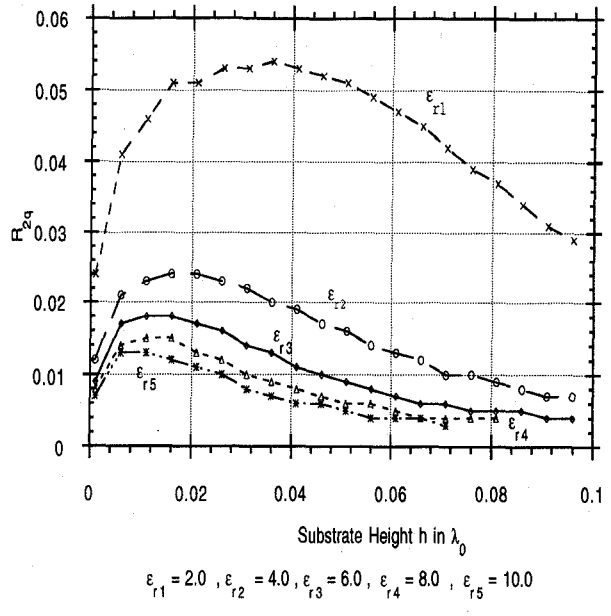

(b)

Fig. 4. (a)–(b) Shows the radius R_{iq} of the region of validity of the quasi-dynamic approximation for different values of h and ϵ_r.

as defined in [14] by

$$G_{1q2} = \frac{e^{-jkr_0}}{r_0} - \frac{e^{-jkr_1}}{r_1}$$

$$G_{2q2} = (1 - \eta)\left\{\frac{e^{-jkr_1}}{r_1} - (1 + \eta)\sum_{i=1}^{i=\infty}(-\eta)^{(i-1)}\frac{e^{-jkr_i}}{r_i}\right\} \tag{14}$$

where the wave number k is defined by

$$e^{-jkr} = \cos(k_1 r) + j \sin(k_2 r) \tag{15}$$

and k_2 is the wave number in medium 2. The definition given by (7) and (8) however, seems to yield the largest region of validity.

2.2 The Asymptotic Approximation

The asymptotic approximations $G_{1a}(\rho)$ and $G_{2a}(\rho)$ for $G_1(\rho)$ and $G_2(\rho)$ are defined as

$$G_{1a}(\rho) = \lim_{\rho \to \infty} G_1(\rho) \tag{16}$$

$$G_{2a}(\rho) = \lim_{\rho \to \infty} G_2(\rho) \tag{17}$$

and though they are defined in the limiting sense as $\rho \to \infty$, they are generally valid to an excellent accuracy for ρ greater than a fraction of a free space wavelength for most practical microstrip circuits [15]. In this paper, the asymptotic solution is obtained by deforming the path of integration in $G_1(\rho)$ and $G_2(\rho)$ to the path of steepest descent and using the first order approximation for the Hankel function, namely

$$\lim_{(\lambda\rho) \to \infty} H_0^2(\lambda\rho) \approx \sqrt{\frac{2}{\pi\lambda\rho}}\, e^{-j\lambda\rho} e^{j(\pi/4)} \tag{18}$$

A detailed description for the derivation of the general expressions for $G_{1a}(\rho)$ and $G_{2a}(\rho)$ can be found in [16]. For completeness, the general expressions for $G_{1a}(\rho)$ and $G_{2a}(\rho)$ are given in the Appendix. For the special case when the frequency of operation is such that

$$f \le \frac{c_0}{4h\sqrt{\epsilon_r - 1}} \tag{19}$$

where c_0 is the speed of light in air, D_{TE} has no poles on the real axis while D_{TM} has only one pole [12], [13]. The expressions for $G_{1a}(\rho)$ and $G_{2a}(\rho)$ then reduce to

$$G_{1a}(\rho) = \frac{-2j \tan^2(k_1 h\sqrt{\epsilon_r - 1})}{\epsilon_r - 1}\frac{e^{-jk_1\rho}}{k_1\rho^2}$$

$$G_{2a} = \left\{\begin{array}{l} 2(1-j)\dfrac{A_{1\mathrm{TM}}}{b_{1\mathrm{TM}}}\dfrac{1}{\rho} \\ \quad + \left[\dfrac{2j(\epsilon_r - 1 - \tan^2(k_1 h\sqrt{\epsilon_r - 1})}{\epsilon_r - 1}\right. \\ \quad \left. + (1-j)\dfrac{A_{1\mathrm{TM}}}{b_{1\mathrm{TM}}^3}\right]\dfrac{1}{k_1\rho^2} \\ \quad + \text{higher order terms} \end{array}\right\} e^{-jk_1\rho} \\ + 2Ak_{1\mathrm{TM}}(1+j)\sqrt{\frac{k_1\pi}{\rho}}\, W(\sqrt{k_1\rho}\, b_{1\mathrm{TM}}) \tag{21}$$

where the parameters of the above equations are given in the Appendix. It is interesting to note that the phase behavior of the asymptotic solution predicted by (20) is the same as the phase predicted by (11). From this it can be concluded that the phase term of the quasi-dynamic approximation (11) is valid for all distances (ρ) at the interface when the substrate height (h) is small compared to the wavelength of the frequency of operation. Further-

more, it was observed in [1] that the quasi-dynamic phase is more accurate, at the interface, in the far field than in the near field. Thus to obtain a more accurate asymptotic representation than (20) we define

$$G_{1a2} = \frac{-2j \tan^2 (k_1 h \sqrt{\epsilon_r - 1})}{\epsilon_r - 1} \frac{e^{-jk_1\rho}}{k_1\rho^2} \cdot \exp\left[j \operatorname{Im}\left(\log\left(\frac{e^{-jk_1\rho_0}}{\rho_0} - \frac{e^{-jk_1\rho_1}}{\rho_1}\right)\right)\right] \quad (22)$$

where Im (x) denotes the imaginary part of x. Thus $G_{1a2}(\rho)$ has the same magnitude as $G_{1a}(\rho)$ but a different phase. The phase of $G_{1a2}(\rho)$ however, is more accurate than that of $G_{1a}(\rho)$. Both equations (20) and (22) have been compared to the dynamic solution for a range of values of h and ϵ_r such that (19) is satisfied and in all cases, it was found that (22) is a better approximation for the dynamic solution than (20). To investigate the accuracy of the asymptotic solution $G_{1a2}(\rho)$, we compare it to the dynamic solution $G_1(\rho)$. For this purpose, we define:

$$R_{1ma} = \left|\frac{G_1(\rho)}{G_{1a2}(\rho)}\right| \quad (23)$$

$$R_{1pa} = \frac{P[G_1(\rho)]}{P[G_{1a2}(\rho)]} \quad (24)$$

where $P[x]$ denotes the phase of the function x. Thus, Figs. 5(a)–(b) show plots of R_{1ma} and R_{1pa} for different values of the microstrip parameters when (19) is satisfied. The region of validity of the asymptotic solution is then defined, similarly to (12), by a Radius R_{ia} such that:

$$\left|\frac{G_i(\rho) - G_{ia}(\rho)}{G_i(\rho)}\right| \leq \text{error for all } \rho \geq R_{ia}. \quad (26)$$

Finally, in order to efficiently evaluate the moment method generalized impedance matrix, we first compute the quasi-dynamic radius R_q and the asymptotic radius R_a subject to a specified error tolerance. The Green's functions $G_1(\rho)$ and $G_2(\rho)$ are then evaluated using the closed form quasi-dynamic solution for $\rho \leq R_q$, the numerical dynamic solution [3], [10] for $R_q \leq \rho \leq R_a$, and finally the closed form asymptotic solution [16] for $\rho \geq R_a$. The numerical dynamic solution is therefore evaluated only in the narrow intermediate field regions. This results in a significant reduction in the computational time particularly in the analysis of electrically large structures [15] as most of the computations occur in the region ($\rho \geq R_a$).

2.3 Extraction of The Frequency Dependent Network Parameters

As described in [1]–[2], in order to define a network description of the microstrip circuit, we define a voltage distribution in terms of the normal component of the electric field. The voltage distribution is thus given by [1]–[3].

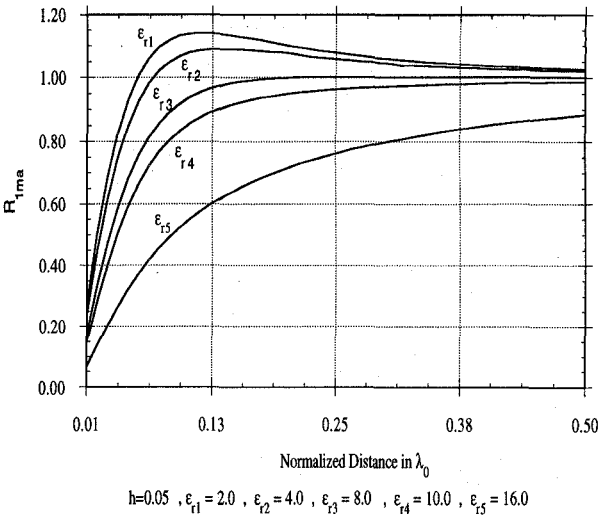

(a)

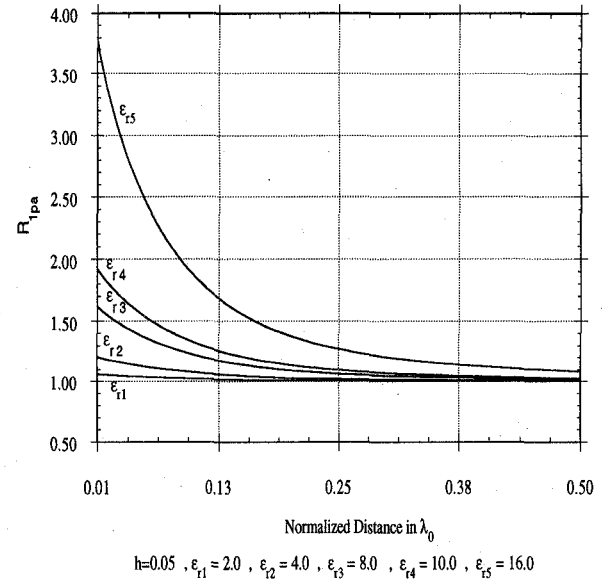

(b)

Fig. 5. (a) Shows a plot of the ratio (R_{1ma}) of the magnitude of the dynamic $G_1(\rho)$ to the magnitude of the asymptotic $G_{1a2}(\rho)$ for different values of h and ϵ_r. (b) Shows a plot of the ratio (R_{1pa}) of the phase of the dynamic $G_1(\rho)$ to the phase of the asymptotic $G_{1a2}(\rho)$ for different values of h and ϵ_r.

$$V(x, y) = \frac{jI}{4\pi\omega\epsilon_1} \int_W dy' Q_y(y') \cdot \int_l \frac{\partial}{\partial x'} J_{sx}(x') G_2(x, y, x', y'). \quad (27)$$

From the voltage and current distributions, the frequency dependent circuit parameters such as the $[S]$, $[Z]$, or $[ABCD]$ parameters can be readily obtained. Specifically, we first define an N-port network by defining N reference planes on the circuit. To illustrate, Fig. 6 shows such a network of 4 signal conductors $C1$, $C2$, $C3$, and $C4$. The N reference planes (P 1–P 8) are defined along the lengths of the lines in the z direction. The network is then excited at one end, quite far from the reference plane ($d \geq 0.1$ λ_0). The obtained voltages and currents at the reference planes are then denoted by (V_{11}, V_{12}, $\cdots$ V_{1n}, I_{11}, I_{12},

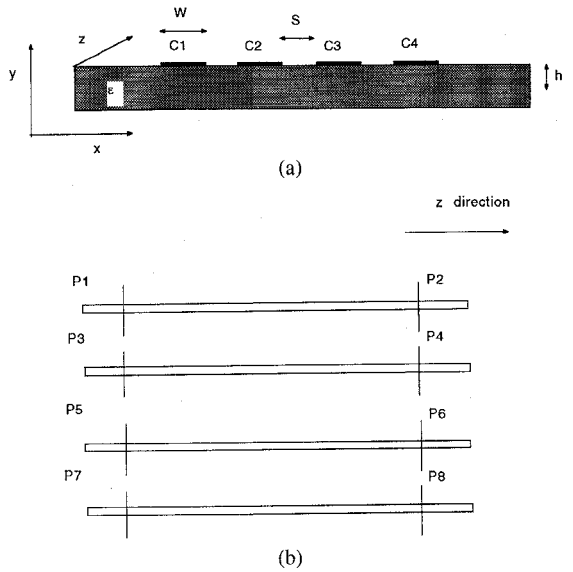

Fig. 6. (a)–(b) Shows the 3-D 8 port network representation of a 4 conductor microstrip transmission line.

$\cdots I_{1n}$). In total, the network is independently excited N times, each time a set of voltages and currents at the N reference planes is obtained. Thus denoting the set of voltages and currents obtained from the ith excitation by ($V_{i1}, V_{i2}, \cdots, V_{\text{in}}, I_{i1}, I_{i2}, \cdots, I_{\text{in}}$), the Z matrix of the N port Network is obtained as:

$$\begin{bmatrix} Z_{11} \\ \vdots \\ Z_{1n} \\ Z_{21} \\ \vdots \\ Z_{2n} \\ \vdots \\ \vdots \\ Z_{n1} \\ \vdots \\ Z_{nn} \end{bmatrix} = \begin{bmatrix} I_{11} & \cdots & I_{1n} & 0 & 0 & 0 & 0 & \cdots & 0^{(n^2\text{th col})} \\ \vdots & & \vdots & \vdots & \vdots & \vdots & \vdots & & \vdots \\ 0^{(n\text{th row})} & 0 & 0 & 0 & 0 & 0 & I_{11} & \cdots & I_{1n}^{(n^2\text{th col})} \\ I_{21} & \cdots & I_{2n} & 0 & 0 & 0 & 0 & \cdots & 0^{(n^2\text{th col})} \\ \vdots & & \vdots & \vdots & \vdots & \vdots & \vdots & & \vdots \\ 0^{(2n\text{th row})} & 0 & 0 & 0 & 0 & \cdots & I_{21} & \cdots & I_{2n} \\ \vdots & & \vdots & \vdots & \vdots & \vdots & \vdots & & \vdots \\ \vdots & & \vdots & \vdots & \vdots & \vdots & \vdots & & \vdots \\ I_{n1} & \cdots & I_{nn} & 0 & 0 & 0 & 0 & \cdots & 0 \\ \vdots & & \vdots & \vdots & \vdots & \vdots & \vdots & & \vdots \\ 0^{(n^2\text{th row})} & 0 & 0 & 0 & 0 & \cdots & I_{n1} & \cdots & I_{nn} \end{bmatrix}^{-1} \begin{bmatrix} V_{11} \\ \vdots \\ V_{1n} \\ V_{21} \\ \vdots \\ V_{2n} \\ \vdots \\ \vdots \\ V_{n1} \\ \vdots \\ V_{nn} \end{bmatrix}. \tag{28}$$

The S parameters can be extracted from the Z parameters using the transformation given by:

$$[S] = [(z + I)]^{-1}[(z - I)] \tag{29}$$

where $[z]$ is the normalized $[Z]$ matrix defined by

$$z_{ij} = \frac{Z_{ij}}{\sqrt{Z_{oi} Z_{oj}}}. \tag{30}$$

Z_{oi} being the characteristic impedance of the line at the ith port and $[I]$ being the identity matrix.

III. Numerical Examples

3.1 Computation of the [S] Parameters of a Uniform Two Conductor Transmission Line

In this example, we solve for the $[S]$ parameters of a uniform two conductor transmission line. The line geometrical and electrical data are shown in Fig. 7. Four ports are then defined quite far from the excitations (Fig. 7(a)) and the sets of voltages and currents at those ports are obtained as described in the previous section. The $[Z]$ parameters are then computed using (28). In order to obtain the $[S]$ parameters of the line, it is necessary to compute the characteristic impedance at each port. The 3-D, frequency dependent, characteristic impedance is computed in the same manner as described in [1]. The $[S]$ parameters are then extracted from the $[Z]$ parameters using (30). In order to check the results of this 3-D modeling, the $[S]$ parameters are then computed using a 2-D approach. In this 2-D approach, the line circuit parameters, that is the inductance matrix $[L]$, the electrostatic induction coefficients matrix $[C]$, and the conductance matrix $[G]$ are computed using a two dimensional analysis of the circuit board cross section [8], [9]. For different frequencies, it is assumed that the inductance and electrostatic induction coefficients matrices remain constant while the conductance matrix $[G]$ varies linearly with frequency [17]. In this 2-D analysis, the resistance matrix $[R]$ of the line is assumed to be zero and all ports are terminated by the 2-D characteristic impedance of the line at the corresponding port. The 3-D and 2-D $[S]$ parameters are computed at 3,

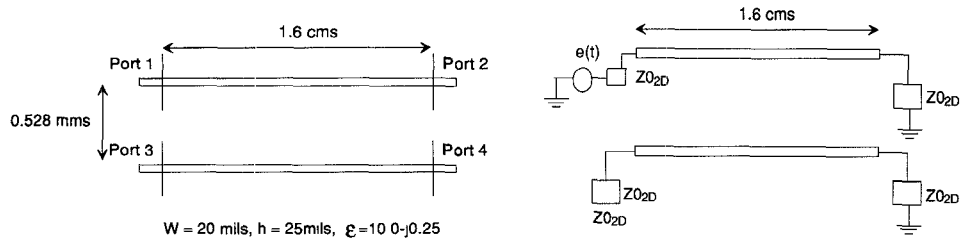

Fig. 7. (a) Shows the 3-D 4 port network representation of a 2 conductor uniform microstrip transmission line. (b) Shows the 2-D quasi-TEM approximation of the circuit in Fig. 7(a).

4, and 5 GHz. These parameters are given by

$f = 3.0$ GHz.

$$[S]^{3D}_{Mag} = \begin{bmatrix} 0.2438E-01 & 0.7326E-01 & 0.9602E+00 & 0.1192E+00 \\ 0.7326E-01 & 0.2438E-01 & 0.1192E+00 & 0.9602E+00 \\ 0.9596E+00 & 0.1191E+00 & 0.2419E-01 & 0.7333E-01 \\ 0.1191E+00 & 0.9596E+00 & 0.7333E-01 & 0.2419E-01 \end{bmatrix}$$

$$[S]^{2D}_{Mag} = \begin{bmatrix} 0.2347E-01 & 0.7890E-01 & 0.9569E+00 & 0.1325E+00 \\ 0.7890E-01 & 0.2347E-01 & 0.1325E+00 & 0.9569E+00 \\ 0.9569E+00 & 0.1325E+00 & 0.2347E-01 & 0.7890E-01 \\ 0.1325E+00 & 0.9569E+00 & 0.7890E-01 & 0.2347E-01 \end{bmatrix}$$

$$[S]^{3D}_{Pha} = \begin{bmatrix} 0.2220E+01 & -0.9652E+00 & -0.2608E+01 & 0.2098E+01 \\ -0.9652E+00 & 0.2220E+01 & 0.2098E+01 & -0.2608E+01 \\ -0.2608E+01 & 0.2098E+01 & 0.2250E+01 & -0.9656E+00 \\ 0.2098E+01 & -0.2608E+01 & -0.9656E+00 & 0.2250E+01 \end{bmatrix}$$

$$[S]^{2D}_{Pha} = \begin{bmatrix} 0.2249E+01 & -0.9814E+00 & -0.2631E+01 & 0.2073E+01 \\ -0.9814E+01 & 0.2294E+01 & 0.2073E+01 & -0.2631E+01 \\ -0.2631E+01 & 0.2073E+01 & 0.2294E+01 & -0.9814E+00 \\ 0.2073E+01 & -0.2631E+01 & -0.9814E+00 & 0.2294E+01 \end{bmatrix}$$

$f = 4.0$ GHz

$$[S]^{3D}_{Mag} = \begin{bmatrix} 0.2813E-01 & 0.6105E-01 & 0.9454E+00 & 0.1549E+00 \\ 0.6105E-01 & 0.2183E-01 & 0.1549E+00 & 0.9454E+00 \\ 0.9446E+00 & 0.1548E+00 & 0.2192E-01 & 0.6113E-01 \\ 0.1548E+00 & 0.9446E+00 & 0.6113E-01 & 0.2192E-01 \end{bmatrix}$$

$$[S]^{2D}_{Mag} = \begin{bmatrix} 0.2283E-01 & 0.7364E-01 & 0.9382E+00 & 0.1788E+00 \\ 0.7364E-01 & 0.2283E-01 & 0.1788E+00 & 0.9382E+00 \\ 0.9382E+00 & 0.1788E+00 & 0.2283E-01 & 0.7364E-01 \\ 0.1788E+00 & 0.9382E+00 & 0.7364E-01 & 0.2283E-01 \end{bmatrix}$$

$$[S]^{3D}_{Pha} = \begin{bmatrix} 0.8850E+00 & 0.9946E+00 & 0.2683E+01 & 0.1097E+01 \\ 0.9946E+00 & 0.8850E+00 & 0.1097E+01 & 0.2683E+01 \\ 0.2683E+01 & 0.1093E+01 & 0.9010E+00 & 0.1005E+01 \\ 0.1093E+01 & 0.2683E+01 & 0.1005E+01 & 0.9010E+00 \end{bmatrix}$$

$$[S]^{2D}_{Pha} = \begin{bmatrix} 0.7125E+00 & 0.9604E+00 & 0.2642E-01 & 0.1050E+00 \\ 0.9604E+00 & 0.7125E+00 & 0.1051E+00 & 0.2642E+01 \\ 0.2642E+01 & 0.1051E+01 & 0.7125E+00 & 0.9604E+00 \\ 0.1051E+01 & 0.2642E+01 & 0.9604E+00 & 0.7125E+00 \end{bmatrix}$$

$f = 5.0$ GHz

$$[S]^{3D}_{Mag} = \begin{bmatrix} 0.1925E-01 & 0.1165E+00 & 0.9309E+00 & 0.1712E+00 \\ 0.1165E+00 & 0.1925E-01 & 0.1712E+00 & 0.9309E+00 \\ 0.9301E+00 & 0.1716E+00 & 0.1943E-01 & 0.1170E+00 \\ 0.1716E+00 & 0.9301E+00 & 0.1170E+00 & 0.1943E-01 \end{bmatrix}$$

$$[S]^{2D}_{Mag} = \begin{bmatrix} 0.2013E-01 & 0.1379E+00 & 0.9187E+00 & 0.2046E+00 \\ 0.1377E-01 & 0.2013E-01 & 0.2046E+00 & 0.9187E+00 \\ 0.9187E+00 & 0.2046E+00 & 0.2013E-01 & 0.1377E+00 \\ 0.2046E+00 & 0.9187E+00 & 0.1377E+00 & 0.2013E-01 \end{bmatrix}$$

$$[S]^{3D}_{Pha} = \begin{bmatrix} -0.9272E-01 & 0.4447E+00 & 0.2060E+01 & 0.4722E+00 \\ 0.4447E+00 & -0.9272E-01 & 0.4722E+00 & 0.2060E+01 \\ 0.2060E+01 & 0.4696E+00 & -0.5139E-01 & 0.4509E+00 \\ 0.4696E+00 & 0.2060E+01 & 0.4509E+00 & -0.5139E-01 \end{bmatrix}$$

$$[S]^{2D}_{Pha} = \begin{bmatrix} -0.8049E+00 & 0.4081E+00 & 0.2006E+01 & 0.4176E+00 \\ 0.4081E+00 & -0.8049E+00 & 0.4176E+00 & 0.2006E+01 \\ 0.2006E+01 & 0.4176E+00 & -0.8049E+00 & 0.4081E+00 \\ 0.4176E+00 & 0.2006E+01 & 0.4081E+00 & -0.8049E+00 \end{bmatrix}$$

As can be seen from the above matrices, there is a good agreement between the 2-D and 3-D solutions. It is interesting to note however, that in the 2-D analysis, the line is 1.6 cms long and is terminated by its characteristic impedance at each port. The line is thus very closely matched. Its behavior is very close to the infinitely long line. In the 3-D analysis however, and due to the choice of basis functions, the current terminates at the line ends presenting an effective infinite impedance. Therefore, in order to have a meaningful comparison between the 3-D and 2-D results, the line ends and excitations must be quite far from the ports in the 3-D case (Fig. 7). In this particular problem, for the 3-D case, the line length is chosen to be 4.0 cms. The ports however, are 1.6 cms apart, symmetrically located from the line ends. This partially accounts for the small difference between the 2-D and 3-D results. It is also interesting to note that, as expected, the agreement is better at lower frequencies since the static solution is a good approximation of the dynamic solution at lower frequencies. The slight asymmetry in the 3-D results are due to the numerical errors incurred in the computation of the voltage and current distributions as well as in the extraction of the circuit parameters.

3.2 Computation of The [S] Parameters of a Tapered Two Conductor Transmission Line

In this example we solve for the [S] parameters of a tapered two conductor transmission line. The line has the same length as the two conductor line of the previous section (4 cms). Its geometrical and electrical data are shown in Fig. 8. A 4-port network is then defined by 4 reference planes 1.6 cms apart and symmetrically located from the port ends. The 3-D frequency dependent [S] parameters of the line are then calculated exactly as described in the previous section. In order to check the results in this case

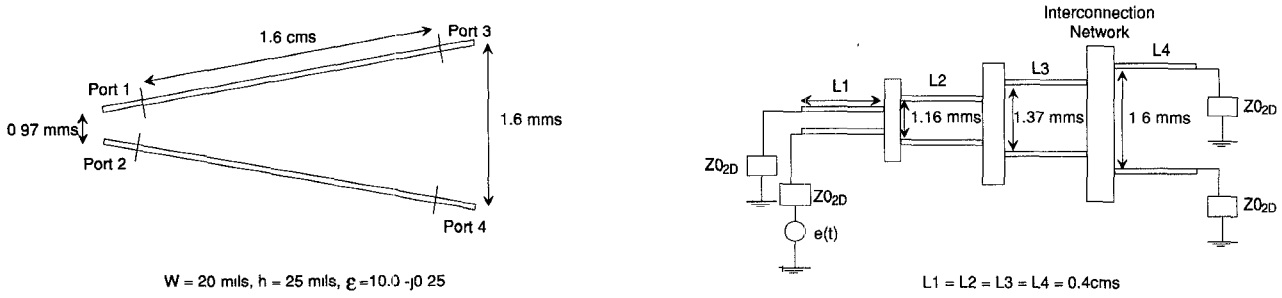

Fig. 8. (a) Shows the 3-D 4 port network representation of a 2 conductor tapered microstrip transmission line. (b) Shows the 2-D quasi-TEM approximation of the circuit in Fig. 8(a).

however, the line is approximated by a cascade of four uniform lines $L1$, $L2$, $L3$, and $L4$. The lines have different separations $S1$, $S2$, $S3$, and $S4$ (Fig. 8(b)). The length of each section is one fourth of the total length of the line (0.4 cms). The 2-D frequency dependent line-circuit parameters $[L]$, $[C]$, and $[G]$ of each section are then computed as described in the previous section. The 2-D $[S]$ parameters of the line are then computed from the individual $[S]$ parameters of each section using standard network theory. The 3-D and 2-D frequency dependent S parameters are computed at 3, 4, and 5 GHz. They are given by

$F = 3$ GHz

$$[S]^{3D}_{Mag} = \begin{bmatrix} 0.3671E-02 & 0.3018E-01 & 0.9669E+00 & 0.7642E-01 \\ 0.3018E-01 & 0.3671E-02 & 0.7642E-01 & 0.9669E+00 \\ 0.9663E+00 & 0.7623E-01 & 0.7253E-02 & 0.2925E-01 \\ 0.7623E-01 & 0.9663E+00 & 0.2925E-01 & 0.7253E-02 \end{bmatrix}$$

$$[S]^{2D}_{Mag} = \begin{bmatrix} 0.3317E-02 & 0.3890E-01 & 0.9646E+00 & 0.8874E-01 \\ 0.3890E-01 & 0.3318E-02 & 0.8874E-01 & 0.9646E+00 \\ 0.9646E+00 & 0.8874E-01 & 0.9832E-02 & 0.3705E-01 \\ 0.8874E-01 & 0.9646E+00 & 0.3705E-01 & 0.9833E-02 \end{bmatrix}$$

$$[S]^{3D}_{Pha} = \begin{bmatrix} 0.1240E+01 & -0.3442E+00 & -0.2625E+01 & 0.2061E+01 \\ -0.3442E+00 & 0.1204E+01 & 0.2061E+01 & -0.2625E+01 \\ -0.2625E+01 & 0.2082E+01 & 0.1302E+01 & -0.1717E+01 \\ 0.2082E+01 & -0.2625E+01 & -0.1717E+01 & 0.1302E+01 \end{bmatrix}$$

$$[S]^{2D}_{Pha} = \begin{bmatrix} 0.1786E+01 & -0.2130E+00 & -0.2649E+01 & 0.2047E+01 \\ -0.2130E+00 & 0.1786E+01 & 0.2047E+01 & -0.2649E+01 \\ -0.2649E+01 & 0.2047E+01 & 0.1492E+01 & -0.1891E+01 \\ 0.2047E+01 & -0.2649E+01 & -0.1891E+01 & 0.1492E+01 \end{bmatrix}$$

$F = 4$ GHz

$$[S]^{3D}_{Mag} = \begin{bmatrix} 0.7891E-02 & 0.2357E-01 & 0.9575E+00 & 0.9179E-01 \\ 0.2357E-01 & 0.7891E-02 & 0.9179E-01 & 0.9575E+00 \\ 0.9573E+00 & 0.9166E-01 & 0.1009E-01 & 0.2049E-01 \\ 0.9166E-01 & 0.9573E+00 & 0.2049E-01 & 0.1009E-01 \end{bmatrix}$$

$$[S]^{2D}_{Mag} = \begin{bmatrix} 0.5214E-02 & 0.3488E-01 & 0.9532E+00 & 0.1138E+00 \\ 0.3488E-01 & 0.5214E-02 & 0.1138E+00 & 0.9532E+00 \\ 0.9532E+00 & 0.1138E+00 & 0.9206E-02 & 0.3098E-01 \\ 0.1138E+00 & 0.9532E+00 & 0.3099E-01 & 0.9208E-02 \end{bmatrix}$$

$$[S]^{3D}_{Pha} = \begin{bmatrix} 0.1685E+01 & 0.5589E+00 & 0.2888E+01 & 0.1301E+01 \\ 0.5589E+00 & 0.1685E+01 & 0.1301E+01 & 0.2888E+01 \\ 0.2888E+01 & 0.1312E+01 & 0.1183E+01 & 0.2006E+01 \\ 0.1312E+01 & 0.2888E+01 & 0.2006E+01 & 0.1183E+01 \end{bmatrix}$$

$$[S]^{2D}_{Pha} = \begin{bmatrix} 0.2205E+01 & 0.4397E+00 & 0.2846E+010 & 0.1262E+01 \\ 0.4397E+01 & 0.2205E+01 & 0.1262E+010 & 0.2846E+01 \\ 0.2846E+01 & 0.1262E+01 & 0.2082E+010 & 0.2082E+01 \\ 0.1262E+01 & 0.2846E+01 & 0.2082E+010 & 0.9590E+00 \end{bmatrix}$$

$F = 5$ GHz

$$[S]^{3D}_{Mag} = \begin{bmatrix} 0.7048E-02 & 0.4577E-01 & 0.9470E+00 & 0.1086E+00 \\ 0.4577E-01 & 0.7048E-02 & 0.1086E+00 & 0.9470E+00 \\ 0.9449E+00 & 0.1079E+00 & 0.4056E-02 & 0.4367E+01 \\ 0.1079E+00 & 0.9449E+00 & 0.4367E-01 & 0.4056E-02 \end{bmatrix}$$

$$[S]^{2D}_{Mag} = \begin{bmatrix} 0.5580E-01 & 0.6218E-01 & 0.9386E+00 & 0.1406E+00 \\ 0.6218E-01 & 0.5581E-02 & 0.1406E+00 & 0.9386E+00 \\ 0.9386E+00 & 0.1406E+00 & 0.3419E-02 & 0.5839E-01 \\ 0.1406E+00 & 0.9386E+00 & 0.5839E-01 & 0.3418E-02 \end{bmatrix}$$

$$[S]^{3D}_{Pha} = \begin{bmatrix} 0.2067E+01 & 0.3745E+00 & 0.2043E+01 & 0.4678E+00 \\ 0.3745E+00 & 0.2067E+01 & 0.4678E+00 & 0.2043E+01 \\ 0.2044E+01 & 0.4681E+00 & 0.1846E+01 & 0.5530E+00 \\ 0.4681E+00 & 0.2044E+01 & 0.5530E+00 & 0.1846E+01 \end{bmatrix}$$

$$[S]^{2D}_{Pha} = \begin{bmatrix} 0.1934E+01 & 0.2880E+00 & 0.1987E+01 & 0.4032E+00 \\ 0.2880E+00 & 0.1934E+01 & 0.4032E+00 & 0.1987E+01 \\ 0.1987E+01 & 0.4032E+00 & -0.3218E+00 & 0.5316E+00 \\ 0.4031E+00 & 0.1987E+01 & 0.5317E+00 & -0.3224E+00 \end{bmatrix}$$

As can be seen from the above matrices the agreement between the 3-D and 2-D results is reasonable.

3.3 Computation of the [S] Parameters of a Half Circle Line

In this section we compute the $[S]$ parameters of a nonuniform transmission line structure consisting of a 1.5 inches long uniform section, a 0.5 inches radius half circle section, and finally a 1.5 inches long uniform section. The line width in this case is 20 mils and the dielectric constant is $10.2 - j0.25$. The geometrical and electrical data are shown in Fig. 9. Before the computation of the frequency dependent $[S]$ parameters of this structure however, we first compute the real part of the propagation constant and thus study the effect of the losses on the line. For this purpose we define two ports, quite far from the excitation and from the half circle discontinuity. The frequency dependent $[Z]$ parameters of the two ports are then computed using (28) and the real part α of the propagation constant is extracted from the $[Z]$ parameters. The real part of the propagation constant is then computed using a 2-D analysis by treating the line as a uniform infinite line. Fig. 10 shows a comparison between the 3-D and 2-D

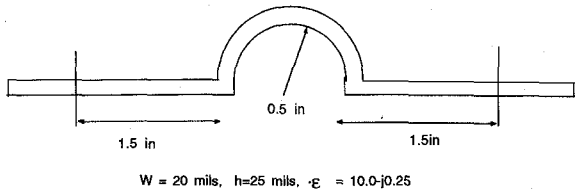

Fig. 9. Shows the 3-D 2 port network representation of a half circle microstrip transmission line.

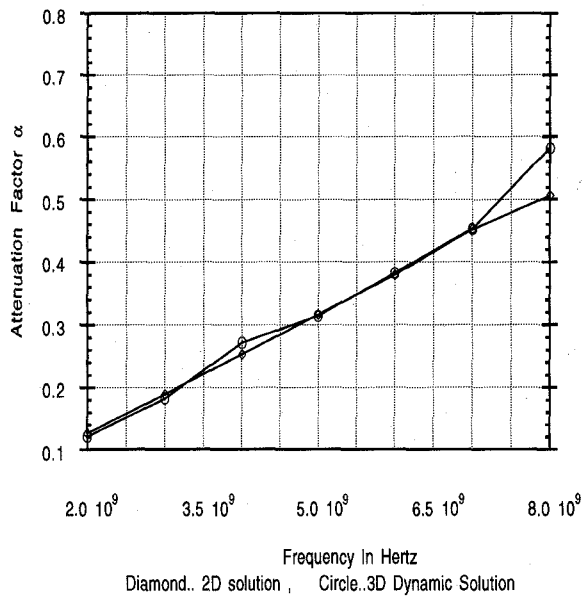

Fig. 10. Shows a comparison between the 3-D dynamic and the 2-D quasi-TEM computation of the frequency dependent attenuation factor α of the line in Fig. 9.

computation of α. The results are almost identical up to 6 GHz and then the 3-D analysis starts predicting higher losses. This is expected due the radiation losses and the finite length of the line resulting in a finite load at the line ends. We next compute the frequency dependent $[S]$ parameters between ports 1 and 2 by first computing the $[Z]$ parameters and then using equation (28). Thus Fig. 11 shows a comparison between the $[S]$ parameters obtained using this 3-D analysis and the experimental data obtained from the HP8510A Network Analyzer. The discrepancy in the magnitude of $[S_{12}]$ and $[S_{21}]$ is about 1.5 dB when the frequency of operation is such that the structure is approximately 10 wavelengths which is about the expected copper loss for this structure.

IV. Conclusion

A new technique, based on a combined approach of using closed form near and far field approximations for the Sommerfeld microstrip Green's functions has been presented. In this technique, the accuracy of the approximations can be set to any desired value. The dynamic Green's functions are evaluated numerically only in the narrow intermediate field regions resulting in a significant reduction of computational time. Finally to check the accuracy of this new technique, several numerical examples have been solved and checked with available data and with experiment.

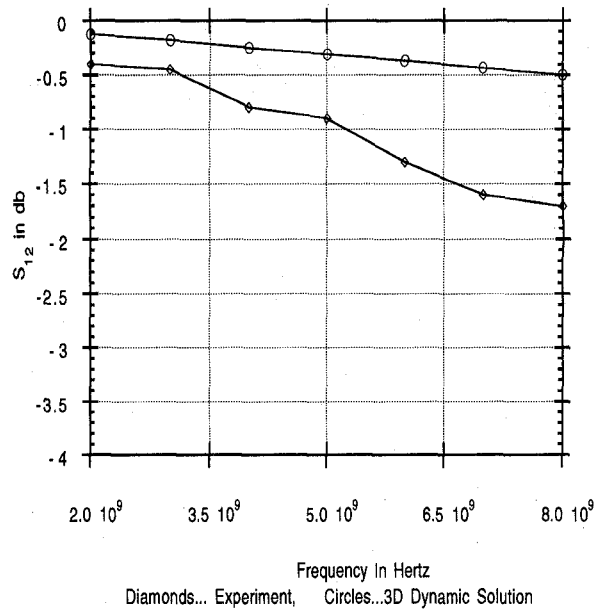

Fig. 11. Shows a comparison between the 3-D theoretical results and the experimental results for the frequency dependent S_{12} parameter of the line in Fig. 9.

Appendix

$$C_1 = -\frac{j\omega\mu I}{4\pi} \tag{A1}$$

$$C_2 = -\frac{jI}{4\pi\omega\epsilon_1} \tag{A2}$$

$$G_1(\rho, \phi) = \int_{k\rho} \frac{H_0^2(k_\rho \rho) k_\rho \, dk_\rho}{D_{\mathrm{TE}}} \tag{A3}$$

$$G_2(\rho, \phi) = \int_{k\rho} \frac{H_0^2(k_\rho \rho) k_\rho N \, dk\rho}{D_{\mathrm{TM}} D_{\mathrm{TE}}} \tag{A4}$$

$$D_{\mathrm{TE}} = \sqrt{k_\rho^2 - k_1^2} + \sqrt{k_\rho^2 - \epsilon_r k_1^2} \coth \left[\sqrt{k_\rho^2 - \epsilon_r k_1^2} h\right] \tag{A5}$$

$$D_{\mathrm{TM}} = \epsilon_{r1} \sqrt{k_\rho^2 - vt k_1^2} + \sqrt{k_\rho^2 - \epsilon_r k_1^2} \tanh \left[\sqrt{k_\rho^2 - \epsilon_r k_1^2} h\right] \tag{A6}$$

$$N = \sqrt{k_\rho^2 - k_1^2} + \sqrt{k_\rho^2 - \epsilon_r k_1^2} \tanh \left[\sqrt{k_\rho^2 - \epsilon_r k_1^2} h\right] \tag{A7}$$

$$G_{1a}(s) = 2(1 - j) \frac{k_1}{\sqrt{\pi}} * \left\{ \sum_{n=1}^{\infty} \left(\frac{1}{n!} F_1^n(0) + \sum_{i=1}^{N_{\mathrm{DTE}}} \frac{A_{i1\mathrm{TE}}}{b_{i\mathrm{TE}}^n} \right) \cdot \frac{\left(\Gamma\left(\frac{1+n}{2}\right)\right)}{\sqrt{\pi}} \right\} \frac{e^{-jk_1\rho}}{(k_1\rho)^{1+(n/2)}} + 2(1 + j) \sqrt{\frac{k_1 \pi}{\rho}} * \left\{ \sum_{i=0}^{N_{\mathrm{DTE}}} A_{i1\mathrm{TE}} W(\sqrt{k_1\rho}\, b_{i\mathrm{TE}}) \right\} \tag{A8}$$

$$G_{2a}(s) = 2(1-j)\frac{k_1}{\sqrt{\pi}} * \left\{ \sum_{n=1}^{\infty} \left(\frac{1}{n!} F_2^n(0) + \sum_{i=1}^{N_{\mathrm{DTE}}} \frac{A_{i2_{\mathrm{TE}}}}{b_{i_{\mathrm{TE}}}^n} + \sum_{i=1}^{N_{\mathrm{DTM}}} \frac{A_{i_{\mathrm{TM}}}}{b_{i_{\mathrm{DTM}}}^n} \right) \frac{\left(\Gamma\left(\frac{1+n}{2}\right)\right)}{\sqrt{\pi}} \right\} \frac{e^{-jk_1\rho}}{(k_1\rho)^{1+(n/2)}}$$

$$+ 2(1+j)\sqrt{\frac{k_1\pi}{\rho}} * \left\{ \sum_{i=0}^{N_{\mathrm{DTE}}} A_{i2_{\mathrm{TE}}} W(\sqrt{k_1\rho}\, b_{i_{\mathrm{TE}}}) + \sum_{i=0}^{N_{\mathrm{DTM}}} A_{i_{\mathrm{TM}}} W(\sqrt{k_1\rho}\, b_{i_{\mathrm{TM}}}) \right\} \tag{A9}$$

$$A_{i1,2_{\mathrm{TE}}} = \frac{j}{2}\sqrt{\lambda_{i_{\mathrm{TE}}}}\, R_{n1,2} \tag{A10}$$

$$A_{i_{\mathrm{TM}}} = \frac{j}{2}\sqrt{\lambda_{i_{\mathrm{DTM}}}}\, R_{n3} \tag{A11}$$

$$R_{n1} = \frac{1}{\frac{\lambda_{n_{\mathrm{TE}}}}{\lambda_{n_{\mathrm{TE}}}^2 - k_1^2} - \frac{\lambda_{n_{\mathrm{TE}}}}{\sqrt{k_1^2\epsilon_r - \lambda_{n_{\mathrm{TE}}}^2}} \cot\left[h\sqrt{k_1^2\epsilon_r - \lambda_{n_{\mathrm{TE}}}^2}\right] + \frac{\lambda_{n_{\mathrm{TE}}} h}{\sin^2\left(h\sqrt{k_1^2\epsilon_r - \lambda_{n_{\mathrm{TE}}}^2}\right)}} \tag{A12}$$

$$R_{n2} = \left(\frac{\sqrt{\lambda_{n_{\mathrm{TE}}}^2 - k_1^2} - \sqrt{k_1^2\epsilon_r - \lambda_{n_{\mathrm{TE}}}^2} \tan\left[h\sqrt{k_1^2\epsilon_r - \lambda_{n_{\mathrm{TE}}}^2}\right]}{\epsilon_r\sqrt{k_{n_{\mathrm{TE}}}^2 - k_1^2} - \sqrt{k_1^2\epsilon_r - \lambda_{n_{\mathrm{TE}}}^2} \tan\left[h\sqrt{k_1^2\epsilon_r - \lambda_{n_{\mathrm{TE}}}^2}\right]} \right) R_{n1} \tag{A13}$$

$$R_{n3} = \left(\frac{\sqrt{\lambda_{n_{\mathrm{TM}}}^2 - k_1^2} - \sqrt{k_1^2\epsilon_r - \lambda_{n_{\mathrm{TM}}}^2} \tan\left[h\sqrt{k_1^2\epsilon_r - \lambda_{n_{\mathrm{TM}}}^2}\right]}{\sqrt{\lambda_{n_{\mathrm{TM}}}^2 - k_1^2} + \sqrt{k_1^2\epsilon_r - \lambda_{n_{\mathrm{TM}}}^2} \cot\left[h\sqrt{k_1^2\epsilon_r - \lambda_{n_{\mathrm{TM}}}^2}\right]} \right)$$

$$* \left(\frac{1}{\frac{\epsilon_r\lambda_{n_{\mathrm{TM}}}}{\sqrt{\lambda_{n_{\mathrm{TM}}}^2 - k_1^2}} + \frac{\lambda_{n_{\mathrm{TM}}}}{\sqrt{k_1^2\epsilon_r - \lambda_{n_{\mathrm{TM}}}^2}} \tan\left[h\sqrt{k_1^2\epsilon_r - \lambda_{n_{\mathrm{TM}}}^2}\right] + \frac{\lambda_{n_{\mathrm{TM}}} h}{\cos^2\left(h\sqrt{k_1^2\epsilon_r - \lambda_{n_{\mathrm{TM}}}^2}\right)}} \right) \tag{A14}$$

$$b_{i_{\mathrm{TE}}} = e^{\pm j(\pi/4)}\sqrt{\lambda_{i_{\mathrm{TE}}} - 1} \tag{A15}$$

$$b_{i_{\mathrm{TM}}} = e^{\pm j(\pi/4)}\sqrt{\lambda_{i_{\mathrm{DTM}}} - 1} \tag{A16}$$

$$W(z) = e^{-z^2}\frac{2}{\sqrt{\pi}}\int_{-z}^{\infty} e^{-t^2}\, dt, \tag{A17}$$

$$F_1(0) = 0 \tag{A18}$$

$$F_1^1(0) = \frac{1}{\sqrt{\epsilon_r - 1}\cot\left(k_1 h\sqrt{\epsilon_r - 1}\right)} \tag{A19}$$

$$F_1^2(0) = 2(1-j)\frac{\tan^2\left(k_1 h\sqrt{\epsilon_r - 1}\right)}{\epsilon_r - 1} \tag{A20}$$

$$F_2(0) = 0 \tag{A21}$$

$$F_2^1(0) = \frac{1}{\epsilon_r - 1\cot\left(k_1 h\sqrt{\epsilon_r - 1}\right)} \tag{A22}$$

$$F_2^2(0) = 2(j-1)\frac{(\epsilon_r - 1 - \tan^2\left(k_1 h\sqrt{\epsilon_r - 1}\right)}{\epsilon_r - 1} \tag{A23}$$

k	Wave Number
k_ρ	Radial Separation Constant.
ω	Angular Frequency.
$\lambda_{n_{\mathrm{TE}}}$	nth pole of D_{TE}.
$\lambda_{n_{\mathrm{TM}}}$	nth pole of D_{TM}
$\lambda_{Rn_{\mathrm{TE}}}$	Real part of the nth pole of D_{TE}.
$\lambda_{Rn_{\mathrm{TM}}}$	Imaginary part of the nth pole of D_{TM}.
$\lambda_{In_{\mathrm{TE}}}$	Real part of the nth pole of D_{TE}.
$\lambda_{In_{\mathrm{TM}}}$	Imaginary part of the nth pole of D_{TM}.

The subscripts 1 and 2 refer to the different media 1 and 2. The $\pm$ sign refer to the surface and leaky wave poles respectively.

ACKNOWLEDGMENT

The authors are grateful to Mr. Real Pomerleau, Ricardo Suarez-Gartner and Tim Schreyer for several enlightening discussions.

REFERENCES

[1] T. R. Arabi, A. T Murphy, T. K. Sarkar, R. F. Harrington, and A. R. Djordjevic, "Analysis of arbitrary oriented microstrip lines and discontinuities utilizing a quasi-dynamic approach," *IEEE Trans. Microwave Theory Tech.*, vol. 39, pp. 75–82, Jan. 1991.

[2] T. R. Arabi, "Dynamic Analysis of Non-uniform Microstrip Multi-Conductor Transmission Lines," Ph.D. dissertation, Syracuse University, Apr. 1991.

[3] J. R. Mosig and T. K. Sarkar, "Comparison of quasi-static and exact electromagnetic fields from a horizontal electric dipole above a lossy dielectric backed by an imperfect ground plane," *IEEE Trans. Microwave Theory Tech.*, vol. MTT-34, pp. 379–387, Apr. 1986.

[4] P. B. Katehi and N. G Alexopoulos, "Frequency dependent characteristics of microstrip discontinuities in millimeter-wave integrated circuits," *IEEE Trans. Microwave Theory Tech.*, vol. MTT-33, no. 10, pp. 1029–1035, Oct., 1985.

[5] J. R. Mosig and F. E. Gardiol, "Integral equation technique for the dynamic analysis of microstrip discontinuities," in *Alta Frequenza*, vol. LYII-N.5, pp. 172–181, June 1988.

[6] M. Kobayashi, "Longitudinal and transverse current distributions on microstrip lines and their closed-form expressions," *IEEE Trans. Microwave Theory Tech.*, vol. MTT-33, pp. 952–959, Oct. 1985.

[7] C. M. Butler, "The equivalent radius of a narrow conducting strip," *IEEE Trans. Antennas Propagat.*, vol. AP-30, no. 4, pp. 755–758, July 1982.

[8] T. R. Arabi, T. K. Sarkar, and A. R. Djordjevic, "Time and frequency domain characterization of multiconductor transmission lines," *J. Electromagn.*, vol. 9 1989, pp. 85–112, Dec. 1989.
[9] C. Wei, R. F. Harrington, J. R. Mautz and T. K. Sarkar, "Multiconductor transmission lines in multilayered dielectric media," *IEEE Trans. Microwave Theory Tech.*, vol. MTT-32, pp. 439–450, Apr. 1984.
[10] J. R. Mosig and F. E. Gardiol, "Analytical and numerical techniques in the Green's function treatment of microstrip antennas and scatterers," *Proc. Inst. Elec. Eng.*, pt. H, vol. 130, no. 2, pp. 175–182, Mar. 1983.
[11] T. Itoh, *Numerical Techniques for Microwave and Millimeter-Wave Passive Structures*. New York: Wiley, 1989.
[12] M. Marin, S. Barkeshli, and P. H. Pathak, "On the location of proper and improper surface wave poles for the grounded dielectric slab," *IEEE Trans. Antennas Propagat.*, vol. 38, pp. 570–573, Apr. 1990.
[13] C.-I. G. Hsu, R. F. Harrington, J. R. Mautz, and T. K. Sarkar, "On the location of leaky wave poles for a grounded dielectric slab," *IEEE Trans. Microwave Theory Tech.*, vol. 39, pp. 346–349, Feb. 1991.
[14] Y. L. Chow and G. E. Howard, "Accurate microstrip computation through minor refinement of the 3-D quasi-dynamic Green's functions," in *Antenna Technology and Applied Electromagnetics*, pp. 103–116, Aug. 1990.
[15] M. Marin, S. Barkeshli, and P. H. Pathak, "Efficient analysis of planar microstrip geometries using a closed-form asymptotic representation of the grounded dielectric slab Green's function," *IEEE Trans. Microwave Theory Tech.*, vol. 37, pp. 669–679, Apr. 1989.
[16] L. B. Felsen and N. Marcuvitz, *Radiation and Scattering of Waves*. Englewood Cliffs, NJ: Prentice-Hall, 1973.
[17] A. R. Djordjevic and T. K. Sarkar, "Analysis of time response of lossy multiconductor transmission line networks," *IEEE Trans. Microwave Theory Tech.*, vol. MTT-35, pp. 898–908, Oct. 1987.

Tawfik R. Arabi (S'91) was born in Beirut Lebanon on Dec. 3, 1964. He received his B.E.E. at the American University of Beirut, Beirut-Lebanon, in June 1985, the M.S. and Ph.D. degrees from Syracuse University, Syracuse, NY in 1987 and 1991, respectively.

He has joined DuPont Electronics while pursing a graduate study during the period of May 1990 to June 1991. Since June 1991, he has been with the Department of Interconnect Technology Development at Intel corporation where he is working on the electromagnetic characterization and circuit optimization of electronic packages in high speed digital systems.

Arthur T. Murphy (S'49–A'54–M'54–SM'61–F'90) received the Ph.D. and M.S. degrees in electrical engineering from Carnegie Mellon University and the B.E.E. degree from Syracuse University.

He established an Electronic Systems Research Group which guides R&D programs by evaluating end-use performance of Du Pont Electronics products. He has expertise in applications in high speed electronic interconnections and electromagnetic interference. He has established a state-of-the-art laboratory and a unique computer-aided design system, called ICONSIMsm, for interconnection simulation. This has been used for designing advanced interconnection assemblies, rigid and flexible printed wiring boards, and ceramic and polymeric packages. He also recently developed a unique thick-film UHF filter which eliminates electromagnetic emissions from computers. He is currently an exchange visiting scientist at the Sony Research Center, Yokohama, Japan, where he is developing high-speed/high-frequency gallium arsenide integrated circuit packages. Before joining Du Pont, 12 years ago, he was Brown Professor and Head of Mechanical Engineering at Carnegie Mellon University and previously held positions of Vice President and Dean of Engineering at Widener University, Head of Electrical Engineering at Wichita State University, Visiting Professor at M.I.T. and the University of Manchester (England), and Adjunct Lecturer at Penn State University.

Dr. Murphy is a Fellow of the AAAS.

Tapan K. Sarkar (S'69–M'76–SM'81) was born in Calcutta, India, on August 2, 1948. He received the B.Tech. degree from the Indian Institute of Technology, Kharagpur, India, in 1969, the M.Sc.E. degree from the University of New Brunswick, Fredericton, Canada, in 1971, and the M.S. and Ph.D. degrees from Syracuse University, Syracuse, NY, in 1975.

From 1975 to 1976 he was with the TACO Division of General Instruments Corporation. He was with the Rochester Institute of Technology, Rochester, NY, from 1976 to 1985. He was a Research Fellow at the Gordon McKay Laboratory, Harvard University, Cambridge, MA, from 1977 to 1978. He is now a Professor in the Department of Electrical and Computer Engineering at Syracuse University. His current research interests deal with the numerical solution of operator equations arising in electromagnetics and signal processing with application to system design. He has authored or coauthored over 154 journal articles and conference papers and has written chapters in eight books.

Dr. Sarkar is a registered professional engineer in the state of New York. He received the Best Paper Award of the IEEE TRANSACTIONS ON ELECTROMAGNETIC COMPATIBILITY in 1979. He also received one of the "best solution" awards in May 1977 at the Rome Air Development Center (RADC) Spectral Estimation Workshop. He was an Associate Editor for feature articles of the IEEE Antennas and Propagation Society Newsletter and the IEEE TRANSACTIONS ON ELECTROMAGNETIC COMPATIBILITY. He was the Technical Program Chairman for the 1988 IEEE Antennas and Propagation Society International Symposium and URSI Radio Science Meeting. Dr. Sarkar is an Associate Editor for the *Journal of Electromagnetic Waves and Applications* and is on the editorial board of the *International Journal of Microwave and Millimeter-Wave Computer Aided Engineering*. He has been appointed U.S. Research Council Representative to many URSI General Assemblies. He is also Chairman of the Intercommission Working Group of International URSI on Time Domain Metrology. He is a member of Sigma Xi and the International Union of Radio Science Commissions A and B.